

# On the Photothermal Response of DNA–Au Core/Shell Nanotoroids as Potential Agents for Photothermal Therapies

Javier González-Colsa, Anton Kuzyk, and Pablo Albella\*

Plasmonic nanoparticles play a pivotal role in various research areas due to their exceptional optical and thermo-optical properties, like high spectral tunability and efficient light-to-heat conversion. Gold, with its biocompatibility, low cytotoxicity, and tunable resonances, makes gold nanoparticles ideal for photothermal therapies. Geometries, including spheres, core–shells, rods, disks, stars, nanocages, and nanotoroids, are extensively studied, with the gold nanodoughnut emerging as one of the most promising ones due to its ability to produce high temperatures and rotational stability. Nevertheless, the fabrication of metallic toroidal shapes remains a challenge. Recent advances in DNA-based nanotechnology, especially DNA-origami techniques, provide a feasible route for the fabrication of this geometry through metallization reactions or attachment of metal nanoparticles. However, particles manufactured using this method possess a DNA core that influences their thermoplasmonic performance. In this work, a theoretical investigation is conducted on the thermoplasmonic response of DNA-origami-based core/shell toroids (CSTs) for photothermal applications. Key parameters that optimize the CST thermoplasmonic response are identified, and compared with their solid counterparts and discrete metallic coatings. Additionally, the CSTs tolerance to random rotations is assessed, providing insights into their behavior in fluidic environments and implications for its practical consideration.

nanocatalysis,<sup>[4]</sup> imaging<sup>[5]</sup> and spectroscopy,<sup>[6]</sup> and information processing,<sup>[7]</sup> among others<sup>[8]</sup> due to their remarkable optical and thermo-optical characteristics. Their main protagonist comes from its ability to concentrate the electromagnetic field at the nanoscale level, owing to the physical phenomenon of localized surface plasmon resonances (LSPRs). An LSPR is a collective coherent oscillation of the free electrons confined in a metallic nanostructure, hence, being closely linked to the AuNPs geometry.<sup>[9–11]</sup> This relation promotes one of the most remarkable properties of LSPR: its spectral tunability. Commonly, big structures or large aspect ratios lead to redshifted spectral plasmonic responses opening the possibility of designing agents to work ad hoc at demanded spectral positions.

The generation of LSPRs is accompanied by a partial reemission of the incident electromagnetic energy (nanoantenna effect), which is the main mechanism of sensing based on nanoparticles. In addition to that, an LSPR causes a partial absorption,


which usually leads to a substantial temperature rise. This behavior effectively converts the AuNPs into both nanoantennae and miniaturized heat sources. Traditionally, researchers tried to minimize or avoid that absorptive nature of nanoantennas to reach strongly enhanced local fields and clean far field signals containing the information of the local targets.<sup>[12]</sup> However, gold nanoplateforms, when acting as nanoheaters, have demonstrated their great potential in a wide range of applications such as enhanced solar light harvesting, drug delivery, or photothermal therapies (PTTs). Hence, big efforts are being made to improve the photoinduced thermal response of metallic nanostructures.<sup>[13–15]</sup> In this work, we focus on the field of PTT, where three factors become especially important: the biocompatibility of the nanostructure materials, the photothermal conversion efficiency of the applied agents and their stability under rotations with respect to the radiation source. These limiting factors provide a well-defined path for the design of nanoheaters oriented to PTTs. First, nanoheaters must be made of biocompatible materials capable of providing a strong plasmonic response. Second, their geometry must support resonances within the so-called near infrared (NIR) biological windows (NIR-I: 700–900 nm and NIR-II: 1000–1400 nm<sup>[16]</sup>) where the

## 1. Introduction

In the recent decades, gold nanoparticles (AuNPs) have played an essential role in various research areas such as nanofluidics,<sup>[1–3]</sup>

J. González-Colsa, P. Albella  
Group of Optics  
Department of Applied Physics  
University of Cantabria  
39005 Santander, Spain  
E-mail: pablo.albella@unican.es

A. Kuzyk  
Department of Neuroscience and Biomedical Engineering  
Aalto University School of Science  
Espoo, Finland

 The ORCID identification number(s) for the author(s) of this article can be found under <https://doi.org/10.1002/ssr.202300523>.

© 2024 The Author(s). Small Structures published by Wiley-VCH GmbH. This is an open access article under the terms of the Creative Commons Attribution License, which permits use, distribution and reproduction in any medium, provided the original work is properly cited.

DOI: 10.1002/ssr.202300523

penetration in the tissue and maximum permissible exposure are maximized. Finally, they must present a reasonable tolerance to rotations.<sup>[17]</sup> It is well known that anisotropic nanoheaters offer different thermal responses depending on their relative orientation with respect to the polarization of the incident beam.<sup>[17–19]</sup> Therefore, it is a fundamental aspect in areas like PTT, where nanoheaters, either free in blood or attached to cells, present a random orientation distribution.

Most of the structures reported in the literature in the context of PTT are entirely or partially built of gold, since it is a biocompatible and nonreactive material with low cytotoxicity. Additionally, it allows the tuning of its resonances within the aforementioned biological windows (NIR-I and NIR-II). Among the most studied and promising geometries are spheres,<sup>[20–23]</sup> core–shells,<sup>[24–26]</sup> rods,<sup>[27–29]</sup> disks,<sup>[30]</sup> stars,<sup>[31,32]</sup> nanocages,<sup>[33]</sup> and nanotoroids.<sup>[17,19]</sup> In recent theoretical studies, we have compared some of these solid structures in an attempt to determine which one may be the most promising for PTT and identified the gold nanodoughnut as an ideal candidate due to its tunability, versatility, and tolerance to rotations.<sup>[17,18]</sup>

Although, in general, metallic nanoparticles of different shapes are routinely fabricated,<sup>[28,34–39]</sup> some geometries are complex and remain challenging. This is the case of the toroid.<sup>[40–42]</sup> Top-down manufacturing methods, such as imprinting lithography,<sup>[43]</sup> colloidal lithography,<sup>[44]</sup> or electron beam lithography,<sup>[45]</sup> have been developed and have demonstrated to be relatively effective in the production of analogous ringlike geometries; however, they are expensive and comparatively low yielding allowing to manufacture toroid-like shapes on substrate only. Molecular self-assembly provides alternative route to large scale bottom-up fabrication of toroidal nanostructures.<sup>[46]</sup> In particular, DNA-origami technique<sup>[47,48]</sup> opens a path for the fabrication of nanoscale toroids with tunable structural parameters. DNA-origami-based toroids can be converted into metal structures either through attachment of metal nanoparticles<sup>[49–51]</sup> or metallization reactions.<sup>[52–56]</sup>

However, one of the main consequences of using DNA origami for the synthesis of metallic nanomaterials, gold nanotoroids in particular, is that their structure is not solid but has a core formed by DNA. This particularity can affect their optical behavior impacting their thermoplasmonic response, which ultimately translates into practical variations of the photothermal efficiency. Thus, given the existing manufacturing limitations for this type of structure and its potential in PTT, it is necessary to assess the influence of this geometric particularity on the thermoplasmonic response of toroidal nanoheaters.

In this work, we conduct a comprehensive theoretical investigation of the thermoplasmonic response exhibited by core/shell toroids (CSTs). Through a systematic study, we identify the key geometrical parameters that optimize the thermoplasmonic response for each proposed structure, contrasting it with its corresponding solid version bearing in mind the target application in PTT. Furthermore, we computationally analyze the potential arrangements of CSTs that can be obtained using the DNA-origami technique. Thus, we examine how the thermal behavior of CSTs changes when it is partially or completely coated with metallic particles, comparing them with the ideal case of a smoothly coated CST. Finally, we explore the behavior of these

structures when they undergo random rotations and understand how this affects their averaged thermoplasmonic response.

## 2. Results

### 2.1. Analysis of the Thermodynamic Behavior of Core/Shell Toroids

The structure under analysis is depicted in **Figure 1**. The structure of CST is composed of a DNA core covered by a gold layer. The optical properties for DNA and gold were taken from refs. [57,58], respectively. To perform the calculations, we have selected the range of geometrical parameters for the CSTs based on arguments coming from either the DNA-origami technique or their applicability in PTTs. The parameters under consideration were the gold thickness ( $\delta_{Au}$ ), the main radius ( $R$ ), and the secondary radius ( $r$ ), as shown in the inset of **Figure 1**. We have fixed the minimum value of  $\delta_{Au} = 5$  nm because, below this thickness, gold undergoes remarkable modifications in its optical properties due to quantum confinement effects on its surface, meaning that the thickness of gold is smaller than the mean free path of electrons. Furthermore, this minimum value of  $\delta_{Au}$  is in good agreement with the thinnest continuous gold shells that can be realized experimentally.<sup>[59,60]</sup> In addition, the maximum gold thickness for each case is linked to the minimum amount of DNA in the CST's core, which has been defined following a toroidal shape with a secondary radius  $r_{DNA} = 5$  nm. The reason for selecting this value is that DNA-origami structures are composed of bundles of double-stranded DNA (dsDNA), and diameter of individual dsDNA is  $\approx 2$  nm. Therefore, a diameter of 10 nm for DNA-origami core is consistent with a lower boundary for this variable. However, this minimum could be lowered without affecting our conclusions, since the structure would be closer to the solid geometry. These two variables impose both a maximum limit on the gold thickness, as well as the minimum size of the CST's secondary radius. The upper limit for the secondary radius is considered as a function of the main radius in such a way that the diametral CST hole has a maximum length of 20 nm. This is because the response of toroids with aspect ratios involving a smaller central hole closely approximates the response of a sphere, offering lower and non-optimized thermal responses, typically outside of the biological windows.<sup>[17]</sup> All this leads to a minimum size of 20 nm for the main radius. Its maximum value is set at 50 nm, as above this value, the thermal response of the nanostructure moves away from the second biological window and goes deeper into the infrared range. The analyzed cases can be seen in **Figure 1**. To interpret this figure, bear in mind that from the experimental point of view, the core diameter is usually fixed so that secondary radius variations come from gold layer thickness modifications. In this study, however, for the sake of comparison with the solid toroid and clarity, we variate both core diameter and gold thickness for a fixed secondary radius.

**Figure 1** shows the absorption spectra for a set of CST configurations excited at normal incidence with a linear polarized plane wave (see **Figure S1 and S2**, Supporting Information, to get more insight on the optical response of these structures). Each column represents variations in main radius for a constant secondary

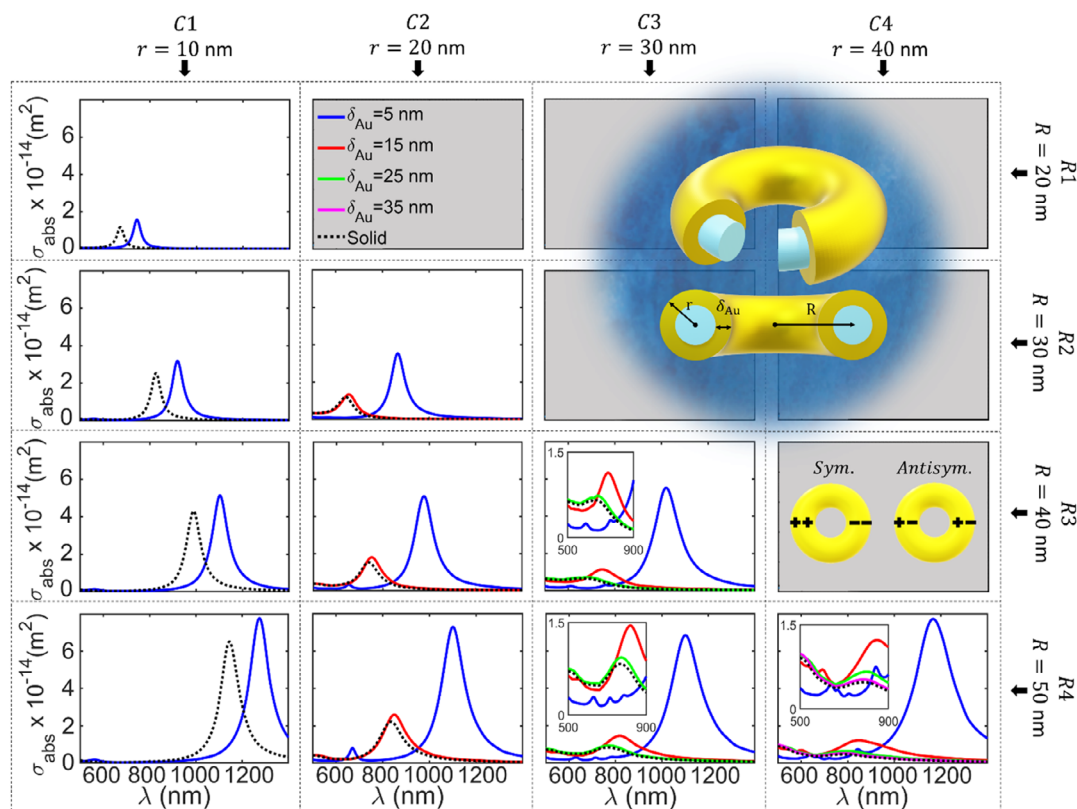


**Figure 1.** Absorption cross section of CSTs as a function of main ( $R$ ), secondary ( $r$ ) radii, and gold thickness ( $\delta_{\text{Au}}$ ). Each column and row represent main radii variations for fixed secondary radii and secondary radii variations for fixed main radii, respectively. The black dotted lines represent the absorption of the solid toroid while blue, red, green, and violet lines represent the CST responses for a gold thickness of 5, 15, 25, and 35 nm, respectively. Inset plots in C3 and C4 highlight the region defined by  $\lambda \in [500, 900]$  nm and  $\sigma_{\text{abs}} \in [0, 1.5] \cdot 10^{-14}$  m<sup>2</sup>.

radius, and each row, the variations in secondary radius for each main radius. From Figure 1, a very well-defined trend is present: first, CST absorption is generally redshifted with respect to the response of the solid structure. This can be explained in terms of the core/shell effect. To illustrate this, the response of solid and core/shell spheres is compared in Figure S2, Supporting Information. As can be seen, the single mode of the core/shell sphere splits into two secondary modes: one being electric dipolar and the other one being electric quadrupolar. As the dipolar response takes advantage of the full length of the structure, it is very sensitive to size variations providing the core/shells structure with an enhanced tunability.

Second, if we look at the columns in Figure 1 (each of it corresponding to a different secondary radius), another trend reveals for both solid and CST: the optical absorption redshifts as main radius grows. This can be understood in terms of the excited electromagnetic modes in ringlike geometries. Solid gold rings often exhibit two main modes, one symmetric and the other antisymmetric, that come from electromagnetic interactions between inner and outer surfaces,<sup>[44]</sup> respectively. The symmetric mode presents a polarization pattern that originates from a strong dipolar excitation involving the entire ring perimeter whose strength is modulated by the interaction of equal sign charges at opposite sides of the walls (see inset in Figure 1). The antisymmetric mode can be explained as the coupling of

two dipoles generated at each ring branch, i.e., an oscillation of opposite charges at each side. Therefore, the symmetric mode (commonly the strongest) is usually redshifted with respect to the asymmetric one and offers higher spectral sensitivity to aspect ratio variations, which provides the ring/toroid geometries with remarkable tunability and optical absorption capabilities.

Lastly, one of the most interesting aspects when comparing solid toroids with CSTs is the trend followed by the electromagnetic response when varying the secondary radii. Looking at row R4 of Figure 1 in the case of solid toroids, the absorption decreases as expected when secondary radius is increased.<sup>[17]</sup> However, when it comes to CSTs, the absorption remains almost stable, only suffering small variations for thin gold coverings (blue lines). This, again, can be reduced to the case of a spherical core/shell (see Figure S3, Supporting Information), where absorption increases when increasing the radius. As shown, this absorption ability is progressively vanishing for increasing gold thicknesses since CSTs approach the solid geometries.

This unexpected performance can be beneficial for PTT since CSTs with thin gold caps offer a remarkable absorption stability under secondary radius imprecisions, in particular core diameter variations, a parameter that can be difficult to control experimentally. Furthermore, in most cases, they present more absorption than their solid versions for all configurations, which promises an enhanced thermoplasmonic response under optical pumping.

Indeed, CSTs present wider responses that become even wider for larger secondary radii (see Figure S3, Supporting Information) something that can result beneficial when multi-spectral light sources are involved. Another potential imperfection that can be induced in CSTs during the manufacturing process is the asymmetric growth.<sup>[61]</sup> It is known that under diffusion limited growth conditions, small particles grow faster than big ones; therefore, a thicker gold cover is expected toward the center of the CST. This effect, as it can be seen in Figure S4, Supporting Information, is more prominent for thick DNA core CSTs. Thus, CSTs with thin cover are stable under this asymmetric shell growth.

As aforementioned, the absorption trend under secondary radius variations is present for all the considered main radii. Therefore, it is enough to analyze the thermal response of the most beneficial configurations, i.e., those defined by  $(R, \delta_{Au}) = (50, 5)$  nm (see Figure S5, Supporting Information, to see the temperature increase for the rest of the configurations). In Figure 2a, the spectral temperature increase of such configurations is compared for both solid toroids and CSTs. In the upper figure, it can be seen that as the secondary radius increases, the thermal response quickly decreases to the extent that it becomes negligible, following the trend marked by the absorption cross section shown in row R4 of Figure 1. In fact,

in most cases, for very small metallic structures compared to the wavelength (quasi-static approximation), the temperature increase often obeys a certain proportionality relationship with the absorption cross section depending on the considered geometry.<sup>[17,18]</sup> Thus, larger absorption cross sections usually lead to higher temperature increases. However, this is not the case for CSTs, as can be seen in the lower representation of Figure 2a. Despite the absorption cross-section features, an almost constant value when increasing the secondary radii (as shown in Figure 1), the temperature notably decreases, qualitatively following a trend closer to that of the solid torus. This particular behavior can be explained in terms of the peculiarities of the geometry itself and how they influence the thermal state.

In this context, a dynamic interplay of multiple factors exerting influence on the thermal dynamics of the structure unfolds. Three factors can be identified: dissipated optical power (heat source, denoted as  $Q$ ), the structural volume, and its surface area. The dependence of the torus temperature increment on these parameters can be modeled by simply solving the heat equation for the case of a sphere,<sup>[22]</sup> but modified to incorporate correction parameters that account for structural features. Thus, the absorption cross section, the equivalent radius of the structure, and a dimensionless coefficient of thermal capacitance come into play (see Section S3, in Supporting Information).

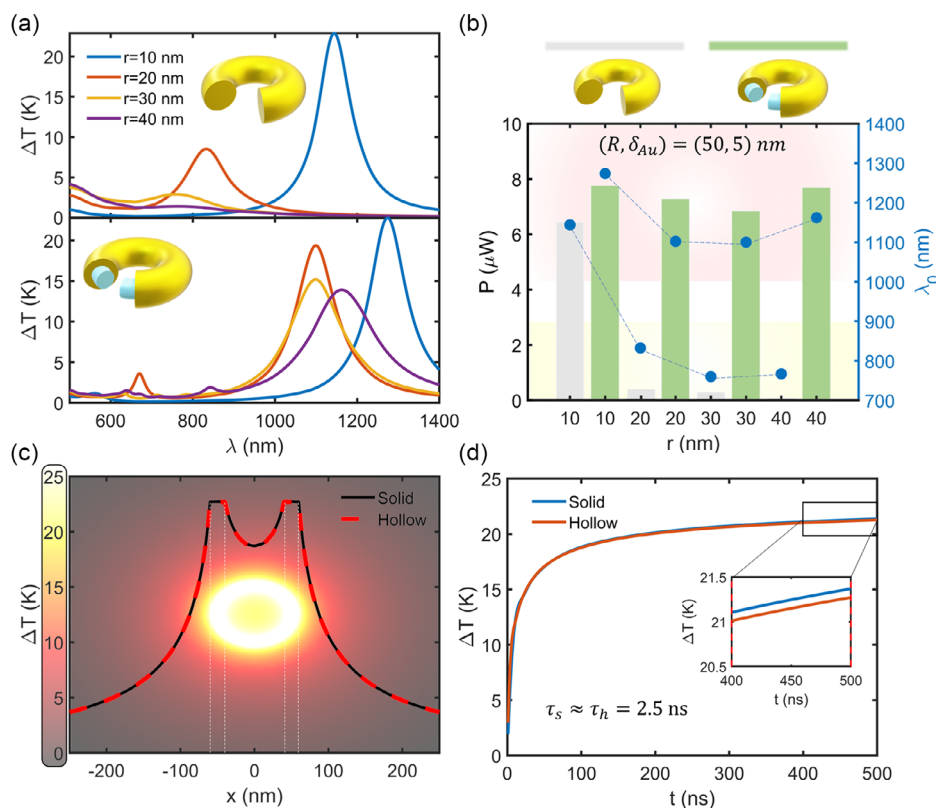


**Figure 2.** a) Temperature increment spectra of gold solid toroids (upper) and CSTs (lower) for a set of secondary radii,  $r = 10, 20, 30$ , and  $40$  nm. b) Dissipated power represented by grey and green boxes respectively (left axis in black) and resonance wavelength (dots corresponding to the right axis in blue) of gold solid toroids and CSTs. The yellowish and reddish regions depict NIR-I and NIR-II regions. c) Spatial distribution taken along the  $x$  axis. The background colormap shows the XY planar section containing the 2D spatial distribution of temperature increment. d) Temporal evolution of the temperature increases for both optimal solid toroid and CST given by  $(R, r) = (50, 10)$  nm and  $(R, r, \delta_{Au}) = (50, 10, 5)$  nm.  $\tau_s$  and  $\tau_h$  are the characteristic heating times of solid toroid and CST from (c) respectively. The input power density is  $I = 0.1 \text{ mW } \mu\text{m}^{-2}$ .



Considering these three variables, a useful quantity with units of thermal flux, that can help to compare the performance of the different geometries, can be defined:  $F = \frac{\sigma_{\text{abs}} I}{R_{\text{eq}} \beta}$ . This, combined with the results for the optical response of both solid toroids and CSTs, allows the reconstruction of the observed trend as seen in Figure S6, Supporting Information. Here, it is demonstrated that the CST produces a higher normalized thermal flux than the solid structure, decreasing for increasing secondary radii in both cases.

Despite this trend in temperature increase, the dissipated power evolves proportionally to the optical absorption as can be seen in Figure 2b. There, it is shown that the optimal CST produces more power than the rest of configurations making this structure superior to its solid counterpart. It is noteworthy that the spectral response of the optimal CSTs lies within the second biological window for all cases. In contrast, solid toroids resonate within NIR-I in most cases, with only one being the optimal in NIR-II. Therefore, as shown in Figure 2a,b, one can deduce that CSTs with thin covers exhibit a remarkable spectral and thermal stability under secondary radii variations compared to their solid versions. This can be decisive during the DNA-origami-based manufacturing process where this variable is often difficult to control.

As shown in Figure 2a,b, an optimal configuration can be selected for each geometry: a solid toroid defined by  $(R, r) = (50, 10)$  nm and a CST defined by  $(R, r, \delta_{\text{Au}}) = (50, 10, 5)$  nm. Thus, their temperature profiles and transient states are calculated in Figure 2c,d. There, it is depicted that both configurations exhibit a similar thermal behavior both spatially and temporally. In the case of the transient response, a very slight difference can be distinguished, as shown in the inset of Figure 2d. This can be explained based on the difference in the amount of metallic mass and the presence of inner face in the case of CSTs. However, this difference is negligible, and by simply fitting the results to a function of the type:  $\Delta T = \Delta T_{\infty}(1 - \text{erf}(\sqrt{\tau/t}))$ ; it can be determined that the characteristic heating time for both structures is approximately  $\tau_s \approx \tau_H = 2.5$  ns. The parameter  $\Delta T_{\infty} \approx 23$  K

is the temperature value obtained in continuous wave simulations, above. Furthermore, from ref. [62], it can be deduced that  $\tau = R^2/4\alpha$ , where  $R$  is the system radius and  $\alpha$  is the thermal diffusivity. Therefore, this theoretical model fits well our values when the water diffusivity and the torus equivalent radius are considered.

## 2.2. Connected Versus Disconnected Shells

So far, we have investigated the optical and thermal response of CSTs and compared their performance with their solid counterparts. We have also estimated the maximum achievable temperature offered by this kind of structure by selecting the optimal configuration in the context of PTT.

However, not only regular hollow particles but also core-shell type structures with disconnected shells can be fabricated by attaching small metal nanoparticles to DNA-origami-based toroids.<sup>[49,51]</sup> Therefore, two questions arise when it comes to this kind of nanostructures: do disconnected toroidal-like shapes exhibit significant and useful thermoplasmonic response? How does that response change with respect to the continuous CST? To address these questions, we have systematically studied the thermoplasmonic response of disconnected CSTs for various metal surface filling percentages ( $\nu$ ), considering the toroidal geometry. We have modelled the disconnected structure as a toroidal DNA core with small AuNPs attached to it. Thus, the degree of surface filling is calculated as the sum of gold sphere circular sections (without considering the intersections when applied) over the core surface area. Consult Figure S7 in Section S4, Supporting Information, to get more insights on the disconnected structure design and implementation in COMSOL Multiphysics.

Figure 3a shows how the disconnected CSTs have been modeled. We started by assuming that spherical particles are distributed around the surface of the DNA core so that particles are progressively added, resulting in a coverage percentage ( $\nu$ ) of 20%, 40%, 60%, 80%, and 100%. This imposes that the number of nanoparticles is  $N_s = 45, 90, 135, 210$  and 421. Since the

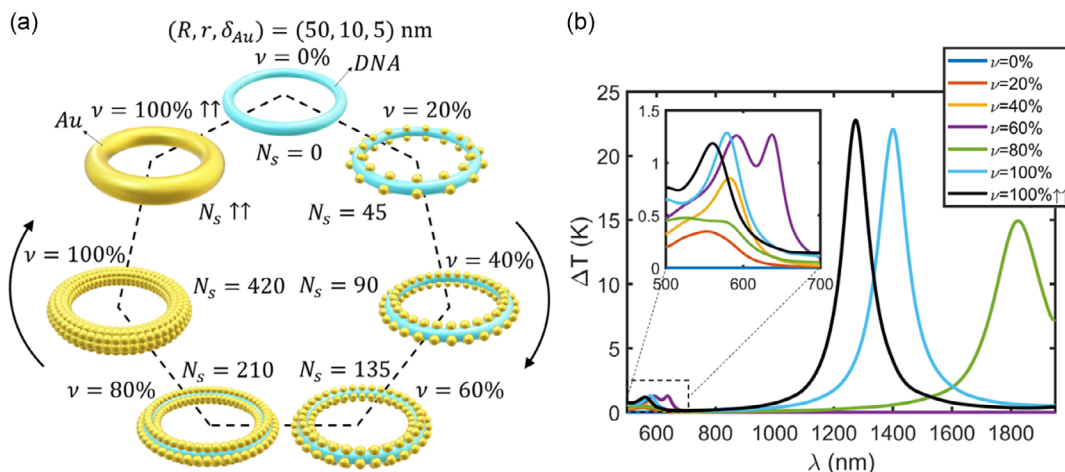


**Figure 3.** a) Representation of the studied CSTs as a function of the surface filling factor ( $\nu$ ) and number of gold spheres ( $N_s$ ). b) Spectral temperature increase of a set of CSTs with  $\nu = 20\%, 40\%, 60\%, 80\%, 100\%$ . The black line, labeled as  $\nu = 100\% \uparrow \uparrow$ , represents the case of the smoothly covered CST with  $(R, r, \delta_{\text{Au}}) = (50, 10, 5)$  nm. The inset highlights the curves between  $\lambda = 500$  nm and  $\lambda = 700$  nm.

coverage percentage is estimated as the sum of the circular cross sections of the gold particles over the total core area, the number of particles grows proportionally to  $\nu$  for low coverage percentages. However, when the distribution is denser, the particle intersections cannot be neglected and this behavior changes, requiring a larger number of particles. This comes from the fact that the estimation of the coverage percentage does not consider the sphere intersecting volumes.

In contrast, as can be seen in Figure 3a, the particles are regularly distributed around the surface of the toroidal core. This results in various possible distributions, given that the parameterization of the surface has two parameters, and there are multiple integer products that approximate the number of particles necessary to achieve a certain coverage percentage (an example is shown in Figure S8, Supporting Information). Therefore, to remove this ambiguity, priority has been given to ensuring that the minimum distance between particles is as big as possible. This is done to reduce the complexity of the structure model in COMSOL, i.e., by having a greater average distance between particles, the volumes of aqueous environment between spheres are larger, allowing relaxation of meshing conditions. This enables both the existence of larger elements (less dense discretization) and higher-quality elements (with lower aspect ratios). In summary, for each situation, the distribution is selected so that it consumes fewer computational resources and ensures greater precision.

Once the distributions are selected, their spectral thermal response is calculated, as shown in Figure 3b. As it can be seen in this figure, the uncovered DNA core ( $\nu = 0\%$ ) does not present thermal response, as expected. This is because DNA does not absorb in the considered spectral region. Furthermore, it can be observed that for values of  $\nu$  below 60%, the thermal response of the system is low compared to the structures considered so far. These responses, as shown in the inset of Figure 3b, qualitatively resemble the response of a single sphere for the cases of  $\nu = 20\%$  and  $\nu = 40\%$ . This is because the distance between particles is significantly large, minimizing the interaction between them, which allows their thermal response to be understood as a sum of each individual response.

Something slightly different happens for  $\nu = 60\%$ : although the thermal response still exhibits a clear maximum qualitatively similar to the response of an isolated sphere, another maximum can be distinguished at longer wavelengths. This can be explained based on the reduction in the average distance between nanoparticles. As they approach each other, they begin to interact, leading to hybridization that gives rise to new modes in the structure.<sup>[50]</sup> Considering the change in temperature, it can be seen that it increases as the surface is covered. This happens because the number of nanoparticles grows as  $\nu$  increases, resulting in a larger volume of gold contributing to the heating.

It is noteworthy that in the case of  $\nu = 80\%$ , a response qualitatively similar to that obtained for the continuous toroid (black line) is achieved. In this case, the number of nanoparticles on the surface is so high that intersections occur between each of the individual volumes, allowing electrons to circulate freely. However, some differences are observed. First, the obtained temperature,  $\Delta T \approx 15$  K, is lower than in the optimal case shown in Figure 3a, where a temperature of  $\Delta T \approx 23$  K was reached. The reason is that we have a large part of the surface covered with

spheres, but the average thickness of the gold coating is smaller due to the geometry of these particles (see Figure S9, Supporting Information). Therefore, the volume of gold is smaller than in the continuous case (black line). In contrast, it can be observed that the response is redshifted ( $\lambda \approx 1800$  nm). This can be explained by considering again the thickness of the gold layer. Although the coverage allows for the presence of an electric dipole mode in the whole toroidal structure, the average thickness is smaller. Consequently, the relative path of the electrons increases, resulting in the observed redshift.<sup>[17]</sup>

Once the structure gets its surface fully covered with AuNPs, the peak temperature increases and the spectral resonance blueshifts approaching the smoothly covered CST response. On the one hand, the temperature increment gets higher ( $\Delta T \approx 22$  K) because of the increase of the number of nanoparticles (larger metallic volume) as well as the structure is able to support the electric dipolar mode across the whole toroidal geometry. Furthermore, the spectral blueshift can be explained based on the average gold thickness: as the number of nanoparticles  $N_s$  increases,  $\delta_{Au}$  approaches the ideal value of  $\delta_{Au} = 5$  nm. An illustrative 2D example on this phenomenon is depicted in Figure S9, Supporting Information. Notice that this study was done over surfaces that are not smooth, having a positive roughness. However, the implications of this parameter have not been considered yet. To address it, a study of roughness has been performed in Section S5, Supporting Information. We have selected the CST structures from row R4 in Figure 1 for  $r = 20, 30, 40$  nm as they present a remarkable absorption while having a thick gold cover. This thick cover is necessary to ensure that, once roughness is included, the local thicknesses do not reduce below 5 nm and the bulk gold optical properties can be applied. As it can be seen in Figure S10, Supporting Information, the rough CSTs have been modeled by a combination of Blender, COMSOL Multiphysics, and Matlab environments. The complexity of the surface makes necessary the use of highly dense meshes to reproduce the curvatures, which imposes a computational limitation of RAM and simulation time. Just to give a figure, the computation of one single rough CST with an optimized mesh over a spectrum of 700–1200 nm takes an average of 36 h. Furthermore, Figure S11, Supporting Information, suggests that, although roughness is an experimental parameter that can be difficult to control and may affect the response of CST structures, it has small significance in its optical response and consequently on its photothermal response. Therefore, the thermal response of these types of structures will remain more or less constant for moderate roughness values, while both the toroidal geometry and its average thickness are maintained to some extent.

In conclusion, as demonstrated in Figure 3, the gold thickness  $\delta_{Au}$  plays a key role in the thermo-optical response of CSTs. Therefore, it needs to be carefully considered and controlled during the fabrication process to get the right structures presenting the desired thermoplasmonic performance.

### 2.3. Thermal Orientation Dependence

We have so far discussed the thermal response of CST, finding a potentially beneficial structure for PTT; however, it is important

to highlight that this happened under the influence of light impinging normally to the plane of the toroid. In fact, the thermal response of anisotropic structures is dramatically affected by the relative orientation to the electromagnetic field of the source.<sup>[17]</sup> In the context of PTT, where the particles will presumably be freely circulating or adhered to cells, it is natural to think that the thermal response of the ensemble of CSTs will not be equivalent to that of an isolated one. For this reason, we conducted a thermal study of the optimal structure proposed in Section 3.1 for different orientations with respect to the incident light, which is assumed to be linearly polarized along  $x$  and  $y$  axes, and circularly polarized. Note that it is common to use a circularly polarized beam to mimic the behavior of nanostructures in the presence of partially or fully unpolarized light.<sup>[17]</sup> Additionally, it is assumed that the excitation wavelength is that at which the CST shows the optimum temperature  $\lambda = 1274$  nm.

**Figure 4** shows the results of the angular thermal mapping of the aforementioned optimal CST for a set of rotations with respect to the  $x$  and  $y$  axes. These rotations are represented by  $\theta$  and  $\phi$  respectively with values between  $0^\circ$  and  $90^\circ$ . As we seek to find the average temperature increment, it is enough to study only one octant, since the source is either linear or circular and the CST presents cylindrical symmetry (see Figure S12, Supporting Information, to see an example of a complete set of rotations). Remark that the green circles refer to a set of evenly distributed points on the sphere (221 points) representing the calculated configurations. Those configurations were obtained by composing two elementary 3D rotation matrices: first, we rotate the CST along  $x$  axis and then along  $y$  axis, starting from normal incidence. The colormaps, however, are just guiding representations obtained by interpolating a denser regular angular mesh (500 points). In other words, we have calculated two sets of configurations for each polarization state. One of them consists of an evenly distributed set of points on the sphere to calculate the average temperature and the other one is a regular mesh in the angular space (non-even distribution on the sphere) to make the interpolation in the planar angular space (see Figure S13 and S14 in Section S6, Supporting Information). Therefore, the conclusions on the CST-averaged thermal response are extracted from the green points.

The main conclusion obtained from Figure 4 is that the polarization state is not relevant to the average thermoplasmonic performance of CSTs if rotations are random. It is important to remark that, by random rotations, we refer to a scenario in which the particle can have all possible orientations either overtime or over the illuminated volume. If this were not the case, a deviation from the average temperature shown here is expected. To illustrate this, imagine there is a driving force defining privileged directions (relative orientations with respect to the light source) due to the geometrical anisotropy of the particle; then, those directions would induce the existence of accumulation points in the unit sphere. This, as discussed in Section S6, Supporting Information, could have big influence on the average thermal response depending on the source-particle configuration. Therefore, in this work, we assume that all relative source-particle orientations are available to the system.

In this way, when the CST is rotated under linearly polarized illumination, its maximum average temperature gets reduced to  $\Delta T_{\text{lin}} \approx 14.8$  K, a reduction of approximately 36% from the optimal configuration (normal incidence). This can be understood by looking at the temperature maps of Figure 4a,b. When light is polarized along  $x$  axis, the temperature map shows a revolution symmetry point around  $(0, 90)$ . This can be explained in terms of the particle-source configuration. For  $(\theta, \phi) = (0, 90)$ , the plane of the toroid is fully transversal to the polarization direction. To illustrate this, if the toroid was ideally modeled by a circle (infinitely thin toroid), the maximum projection of the toroidal diameter onto the  $x$  axis would present the trend shown in Figure 4a (see Figure S15a, Supporting Information). Therefore, the dipolar mode cannot be excited, and no temperature increment is achieved. The opposite takes place when we go far away from that particular point in the planar angular space: the particle maximum length is getting aligned with the polarization direction, enabling the dipolar excitation and giving rise to a strong temperature increment. Indeed, the system performs in a similar way for the reference coordinates  $(0, 0)$ ,  $(90, 0)$ , and  $(90, 90)$  as can be seen in Figure 4a.

Something similar happens when the illumination is polarized along the  $y$  axis (Figure 4b). As the toroid rotates along  $x$  axis (increasing  $\theta$ ), the incident electric field gets progressively

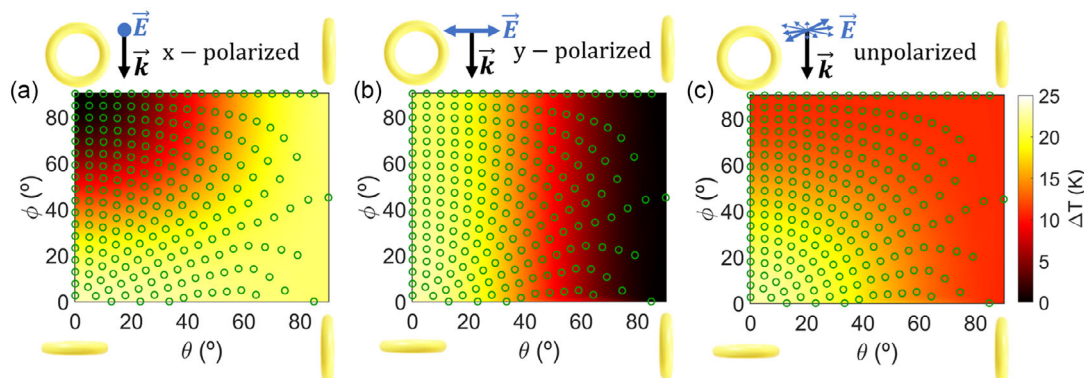


**Figure 4.** Angular thermal mapping of a CST defined by  $(R, r, \delta_{\text{Au}}) = (50, 10, 5)$  nm for linearly polarized incidence along a) the  $x$  and b)  $y$  axes, and c) circularly polarized light polarizations.  $\theta$  and  $\phi$  are rotation angles with respect to the  $x$  and  $y$  axis, respectively. The green circles correspond to the angular sampling taken on the sphere. Insets: particle-light configuration for the corner angular coordinates, namely  $(\theta, \phi)^\circ = (0, 0)^\circ, (0, 90)^\circ, (90, 0)^\circ$ , and  $(90, 90)^\circ$ .



orthogonal to the plane of the toroid, reducing its thermal response. Regarding rotations along  $y$  axis, this geometry presents a remarkable stability. Temperature change is minimal for  $\phi$  variations when  $\theta$  is fixed. This is because its geometrical projection of the toroid diameter on the polarization direction remains almost constant so that the electric field always sees an approximately constant toroidal section. As in the previous case, this can also be supported by considering a circle to ideally represent the toroidal shape. If we project the toroidal (circle) diameter onto the  $y$  axis (polarization direction), it is found that it does not depend on  $\phi$  but on  $\theta$  as can be seen in Section S6, Supporting Information. Indeed, it follows a  $\cos(\theta)$  function type as demonstrated in Figure S15b, Supporting Information.

In contrast, when the toroid is rotating under circularly polarized illumination, the average temperature also reduces to  $\Delta T_{\text{circ}} \approx 14.8$  K approximately. This again can be supported by the fact that rotations are random so that the same reduction in temperature is expected. However, the thermal map shows a different pattern (see Figure 4c). The angular colormap presents cylindrical symmetry indicating that the pair  $(\theta, \phi)$  is unordered as far as temperature is concerned, i.e.,  $T(\theta, \phi) = T(\phi, \theta)$  for all  $\theta, \phi \in [0, 90]^\circ$ . This can be clarified by relying on the polarization state. As the illumination is circularly polarized, the electric field is rotating overtime in such a way that there always exists a configuration in which the toroidal diameter is parallel to the electric field. This allows for a continuous excitation of the dipolar mode. However, each time this excitation occurs, the opposite takes place. This imposes a compromise between both configurations giving rise to the observed reduction in averaged temperature and rotation stability. As in the previous cases, this can also be understood in terms of the CST misalignment with respect to the light polarization plane (see Figure S16, Supporting Information).

### 3. Conclusion

In this work, we have conducted a numerical investigation on the photothermal response of Au–DNA CSTs. We optically studied a broad casuistry to show that this particular geometry generally presents significantly higher temperature increases compared with their solid counterparts. Most of the studied thinly covered CSTs resonate in NIR-II, which provides these structures with a superior performance in PTT applications. Furthermore, we found an optimal CST configuration  $(R, r, \delta_{\text{Au}}) = (50, 10, 5)$  nm that offers the same peak temperature than the solid one but resonating this time at longer wavelengths within NIR-II for normal incidence. This results in a more beneficial structure regarding PTT since this wavelength guarantees larger penetration lengths. We have also analyzed the impact of nanoparticle fabrication stages in the context of DNA-origami technique. Since small metallic nanoparticles are attached to the DNA core to form the shell during the process, the final structure can be disconnected at certain stages. We have shown that a coerture of particles of at least 80% is necessary for the disconnected CST to behave as a continuous shell structure as long as the metallic particles touch each other. Therefore, DNA cores do not need to be fully covered for featuring an electric dipolar mode (typical in solid toroids). This study also reveals the gold thickness as a

key parameter to control during the manufacturing process. In contrast, we have assessed the impact of random rotations on the CST thermal behavior. This nanoparticle shape presents a high tolerance to rotations, a behavior that does not depend on the polarization state of the incident light. It features a minimum temperature reduction with respect to the peak temperature of about 36%, demonstrating its high stability to rotations. Although in this study, we limited our investigation to dimensions that keep the plasmonic resonance within NIR-II; following the recommendations in biomedical applications, these structures can also be relevant candidates in other spectral regions out of NIR-I–II. This makes them suitable for other applications. Therefore, our study, while focused on biological applications, has the potential to be easily extended to other domains by simply finding the appropriate nanoheater materials and subsequent spectral photothermal optimization.

### 4. Experimental Section

Since this work was conducted from a theoretical perspective, we relied on the resolution of the heat diffusion equation to analyze the response of CSTs. To guarantee the reliability of the solutions, we use COMSOL Multiphysics. The procedure consisted of two steps namely light–matter interaction and heat diffusion. Initially, we solved the electromagnetic problem to determine the distribution of resistive losses; specifically, we solved Maxwell's equations using the radiofrequency COMSOL suite. In this process, we defined the CST structure immersed in water, the whole system being surrounded by perfect matched layer boundary conditions. The illumination was fixed to a linearly polarized plane wave with a power density of  $I = 0.1 \text{ mW } \mu\text{m}^{-2}$ , as usual in stationary thermoplasmonic calculations. Furthermore, the discretization was done by employing a free tetrahedral mesh with element sizes adapted according to the excitation wavelength. This guaranteed a dense element distribution and reliable curvatures where necessary. Typically, a maximum allowed mesh size smaller than  $\lambda/5$  was recommended;<sup>[63]</sup> however, in our scenario, we restricted this value to  $\lambda/8$  to fit the quality requirements for each of the studied CST configurations. In addition, Lumerical FDTD was employed to confirm the electromagnetic simulations as it implements a different domain meshing protocol (rectangular mesh distribution).

As for the thermodynamic calculations, we used the heat transfer in solids interface. We considered a heat flux node along the outer boundaries, incorporating a heat transfer coefficient that depended on the geometry and ambient conditions. In our case, we used the built-in Nusselt correlations for plane interfaces which possessed an analytical expression. In this step, we primarily considered conduction as the main transfer mechanism, since we examined small structures within a small amount of fluid under low temperature variations. Furthermore, we did not consider the effect of interfacial thermal conductance as, in the steady state, this parameter would raise the internal temperature without impacting the external one, leading to similar fluid heating.<sup>[23]</sup>

### Supporting Information

Supporting Information is available from the Wiley Online Library or from the author.

### Acknowledgements

This work was financed by the Spanish Ministerio de Ciencia e Innovación under project MOPHOSYS (grant no. PID2022-139560NB-I00). J.G.-C. thanks the Spanish Ministerio de Ciencia e Innovación for his FPI grant and P.A. acknowledges funding for a Ramon y Cajal Fellowship (grant no. RYC-2016-20831). A.K. acknowledges support from the Jane and Aatos



Erkko Foundation and the Academy of Finland Flagship Programme (grant no. 320167 [PREIN Flagship—Aalto University]).

## Conflict of Interest

The authors declare no conflict of interest.

## Data Availability Statement

Data sharing is not applicable to this article as no new data were created or analyzed in this study.

## Keywords

absorption, DNA origami, photothermal, plasmonics, toroids, thermoplasmonics

Received: November 29, 2023

Revised: May 13, 2024

Published online: June 17, 2024

- [1] A. R. Mallah, M. N. Mohd Zubir, O. A. Alawi, K. M. Salim Newaz, A. B. Mohamad Badry, *Sol. Energy Mater. Sol. Cells* **2019**, 201, 110084.
- [2] B. Wang, X. Wang, W. Lou, J. Hao, *J. Colloid Interface Sci.* **2011**, 362, 5.
- [3] L. M. Moreira, E. A. Carvalho, M. J. V. Bell, V. Anjos, A. C. Sant'Ana, A. P. P. Alves, B. Fragneaud, L. A. Sena, B. S. Archanjo, C. A. Achete, *J. Therm. Anal. Calorim.* **2013**, 114, 557.
- [4] Y. Wang, E. Laborda, K. Tschulik, C. Damm, A. Molina, R. G. Compton, *Nanoscale* **2014**, 6, 11024.
- [5] C. J. Murphy, A. M. Gole, J. W. Stone, P. N. Sisco, A. M. Alkilany, E. C. Goldsmith, S. C. Baxter, *Acc. Chem. Res.* **2008**, 41, 1721.
- [6] F. Verger, T. Pain, V. Nazabal, C. Boussard-Plédel, B. Bureau, F. Colas, E. Rinnert, K. Boukerma, C. Compère, M. Guilloix-Viry, S. Deputier, A. Perrin, J. P. Guin, *Sens. Actuators, B* **2012**, 175, 142.
- [7] D. Cotter, R. J. Manning, K. J. Blow, A. D. Ellis, A. E. Kelly, D. Nessel, I. D. Phillips, A. J. Poustie, D. C. Rogers, *Science* **1999**, 286, 1523.
- [8] A. Oyelere, *Nanotechnol. Sci. Appl.* **2008**, 1, 45.
- [9] V. Amendola, R. Pilot, M. Frasconi, O. M. Maragò, M. A. Iatì, *J. Phys. Condens. Matter* **2017**, 29, 203002.
- [10] V. Giannini, A. I. Fernández-Domínguez, S. C. Heck, S. A. Maier, *Chem. Rev.* **2011**, 111, 3888.
- [11] E. Ringe, M. R. Langille, K. Sohn, J. Zhang, J. Huang, C. A. Mirkin, R. P. Van Duyne, L. D. Marks, *J. Phys. Chem. Lett.* **2012**, 3, 1479.
- [12] S. K. Özdemir, G. Turhan-Sayan, *J. Lightwave Technol.* **2003**, 21, 805.
- [13] J. J. Hu, Y. J. Cheng, X. Z. Zhang, *Nanoscale* **2018**, 10, 22657.
- [14] B. Yang, C. Li, Z. Wang, Q. Dai, *Adv. Mater.* **2022**, 34, 2107351.
- [15] J. González-Colsa, J. D. Olarte-Plata, F. Bresme, P. Albella, *J. Phys. Chem. Lett.* **2022**, 13, 6230.
- [16] W. Feng, X. Han, R. Wang, X. Gao, P. Hu, W. Yue, Y. Chen, J. Shi, *Adv. Mater.* **2019**, 31, 1805919.
- [17] J. González-Colsa, G. Serrera, J. M. Saiz, D. Ortiz, F. González, F. Bresme, F. Moreno, P. Albella, *Opt. Express* **2022**, 30, 125.
- [18] J. González-Colsa, A. Franco, F. Bresme, F. Moreno, P. Albella, *Sci. Rep.* **2022**, 12, 14222.
- [19] F. Alali, I. H. Karamelas, Y. H. Kim, E. P. Furlani, *J. Phys. Chem. C* **2013**, 117, 20178.
- [20] A. O. Govorov, W. Zhang, T. Skeini, H. Richardson, J. Lee, N. A. Kotov, *Nanoscale Res. Lett.* **2006**, 1, 84.
- [21] A. O. Govorov, H. H. Richardson, *Nano Today* **2007**, 2, 30.
- [22] G. Baffou, R. Quidant, F. J. García De Abajo, *ACS Nano* **2010**, 4, 709.
- [23] K. Metwally, S. Mensah, G. Baffou, *J. Phys. Chem. C* **2015**, 119, 28586.
- [24] C. Ayala-Orozco, C. Urban, M. W. Knight, A. S. Urban, O. Neumann, S. W. Bishnoi, S. Mukherjee, A. M. Goodman, H. Charron, T. Mitchell, M. Shea, R. Roy, S. Nanda, R. Schiff, N. J. Halas, A. Joshi, *ACS Nano* **2014**, 8, 6372.
- [25] D. P. O'Neal, L. R. Hirsch, N. J. Halas, J. D. Payne, J. L. West, *Cancer Lett.* **2004**, 209, 171.
- [26] A. R. Rastinehad, H. Anastos, E. Wajswol, J. S. Winoker, J. P. Sfakianos, S. K. Doppalapudi, M. R. Carrick, C. J. Knauer, B. Taouli, S. C. Lewis, A. K. Tewari, J. A. Schwartz, S. E. Canfield, A. K. George, J. L. West, N. J. Halas, *Proc. Natl. Acad. Sci. U. S. A.* **2019**, 116, 18590.
- [27] Y. Wang, K. C. L. Black, H. Luehmann, W. Li, Y. Zhang, X. Cai, D. Wan, S. Y. Liu, M. Li, P. Kim, Z. Y. Li, L. V. Wang, Y. Liu, Y. Xia, *ACS Nano* **2013**, 7, 2068.
- [28] J. Pérez-Juste, I. Pastoriza-Santos, L. M. Liz-Marzán, P. Mulvaney, *Coord. Chem. Rev.* **2005**, 249, 1870.
- [29] J. Morales-Dalmau, C. Vilches, I. De Miguel, V. Sanz, R. Quidant, *Nanoscale* **2018**, 10, 2632.
- [30] G. Baffou, R. Quidant, *Laser Photonics Rev.* **2013**, 7, 171.
- [31] P. Senthil Kumar, I. Pastoriza-Santos, B. Rodríguez-González, F. Javier García De Abajo, L. M. Liz-Marzán, *Nanotechnology* **2008**, 19, 015606.
- [32] R. Rodríguez-Oliveros, J. A. Sánchez-Gil, *Opt. Express* **2012**, 20, 621.
- [33] L. Jauffred, A. Samadi, H. Klingberg, P. M. Bendix, L. B. Oddershede, *Chem. Rev.* **2019**, 119, 8087.
- [34] Y. Zheng, X. Zhong, Z. Li, Y. Xia, *Part. Part. Syst. Character.* **2014**, 31, 266.
- [35] A. M. Schwartzberg, T. Y. Olson, C. E. Talley, J. Z. Zhang, *J. Phys. Chem. B* **2006**, 110, 19935.
- [36] C. G. Khoury, T. Vo-Dinh, *J. Phys. Chem. C* **2008**, 112, 18849.
- [37] S. E. Skrabalak, J. Chen, Y. Sun, X. Lu, L. Au, C. M. Cobley, Y. Xia, *Acc. Chem. Res.* **2008**, 41, 1587.
- [38] L. Lu, G. Burke, I. Halaciuga, D. V. Goia, *J. Colloid Interface Sci.* **2013**, 392, 90.
- [39] L. Scarabelli, A. Sánchez-Iglesias, J. Pérez-Juste, L. M. Liz-Marzán, *J. Phys. Chem. Lett.* **2015**, 6, 4270.
- [40] M. Prieto, R. Arenal, L. Henrard, L. Gomez, V. Sebastian, M. Arruebo, *J. Phys. Chem. C* **2014**, 118, 28804.
- [41] T. H. Chow, Y. Lai, X. Cui, W. Lu, X. Zhuo, J. Wang, *Small* **2019**, 15, 1.
- [42] H. J. Jang, S. Ham, J. A. I. Acapulco, Y. Song, S. Hong, K. L. Shuford, S. Park, *J. Am. Chem. Soc.* **2014**, 136, 17674.
- [43] S. Kim, J. M. Jung, D. G. Choi, H. T. Jung, S. M. Yang, *Langmuir* **2006**, 22, 7109.
- [44] J. Aizpurua, P. Hanarp, D. S. Sutherland, M. Käll, G. W. Bryant, F. J. García de Abajo, *Phys. Rev. Lett.* **2003**, 90, 4.
- [45] F. Hao, P. Nordlander, M. T. Burnett, S. A. Maier, *Phys. Rev. B: Condens. Matter Mater. Phys.* **2007**, 76, 245417.
- [46] Y. Kim, W. Li, S. Shin, M. Lee, *Acc. Chem. Res.* **2013**, 46, 2888.
- [47] P. W. K. Rothmund, *Nature* **2006**, 440, 297.
- [48] S. Dey, C. Fan, K. V. Gothelf, J. Li, C. Lin, L. Liu, N. Liu, M. A. D. Nijenhuis, B. Saccà, F. C. Simmel, H. Yan, P. Zhan, *Nat. Rev. Methods Primers* **2021**, 1, <https://doi.org/10.1038/s43586-020-00009-8>.
- [49] R. Schreiber, S. Kempter, S. Holler, V. Schüller, D. Schiffels, S. S. Simmel, P. C. Nickels, T. Liedl, *Small* **2011**, 7, 1795.
- [50] E. M. Roller, L. K. Khorashad, M. Fedoruk, R. Schreiber, A. O. Govorov, T. Liedl, *Nano Lett.* **2015**, 15, 1368.
- [51] M. J. Urban, P. K. Dutta, P. Wang, X. Duan, X. Shen, B. Ding, Y. Ke, N. Liu, *J. Am. Chem. Soc.* **2016**, 138, 5495.
- [52] M. Xie, W. Fang, Z. Qu, Y. Hu, Y. Zhang, J. Chao, J. Shi, L. Wang, L. Wang, Y. Tian, C. Fan, H. Liu, *Nat. Commun.* **2023**, 14, <https://doi.org/10.1038/s41467-023-37333-y>.

- [53] S. Jia, J. Wang, M. Xie, J. Sun, H. Liu, Y. Zhang, J. Chao, J. Li, L. Wang, J. Lin, K. V. Gothelf, C. Fan, *Nat. Commun.* **2019**, *10*, <https://doi.org/10.1038/s41467-019-13507-5>.
- [54] M. M. Islam, M. M. Hossen, J. Adjasoo, P. E. Palo, L. Bendickson, N. E. Kallmyer, N. F. Reuel, M. Nilsen-Hamilton, T. Koschny, A. C. Hillier, *J. Phys. Chem. C* **2023**, *127*, 24291.
- [55] N. Li, Y. Shang, R. Xu, Q. Jiang, J. Liu, L. Wang, Z. Cheng, B. Ding, *J. Am. Chem. Soc.* **2019**, *141*, 17968.
- [56] X. Dai, X. Chen, X. Jing, Y. Zhang, M. Pan, M. Li, Q. Li, P. Liu, C. Fan, X. Liu, *Angew. Chem., Int. Ed.* **2022**, *61*, e202114190.
- [57] T. Inagaki, R. N. Hamm, E. T. Arakawa, L. R. Painter, *J. Chem. Phys.* **1974**, *61*, 4246.
- [58] P. B. Johnson, R. W. Christy, *Phys. Rev. B* **1972**, *6*, 4370.
- [59] L. Lermusiaux, M. Plissonneau, L. Bertry, G. L. Drisko, V. Buisette, T. Le Mercier, E. Duguet, M. Tréguer-Delapierre, *Sci. Rep.* **2021**, *11*, <https://doi.org/10.1038/s41598-021-97171-0>.
- [60] X. Zhang, L. Guo, J. Luo, X. Zhao, T. Wang, Y. Li, Y. Fu, *ACS Appl. Mater. Interfaces* **2016**, *8*, 9889.
- [61] N. T. K. Thanh, N. Maclean, S. Mahiddine, *Chem. Rev.* **2014**, *114*, 7610.
- [62] G. Baffou, *Thermoplasmonics*, Cambridge University, Cambridge **2018**.
- [63] COMSOL Multiphysics V. 6.1. COMSOL AB, Stockholm, Swiden, **2022**, pp. 90–92.